Real-space dynamical mean-field theory of Friedel oscillations in strongly correlated electron systems

B. Chatterjee,[1] J. Skolimowski,[2] K. Makuch,[3] and K. Byczuk ⓘ[4,*]

[1]*Institute of Physics, Czech Academy of Sciences, Na Slovance 2, 182 21 Prague, Czech Republic*
[2]*Scuola Internazionale Superiore di Studi Avanzati (SISSA), Via Bonomea 265, I-34136 Trieste, Italy*
[3]*Institute of Physical Chemistry, Polish Academy of Sciences, Kasprzaka 44/52, 01-224 Warszawa, Poland*
[4]*Institute of Theoretical Physics, Faculty of Physics, University of Warsaw, ul. Pasteura 5, 02-093 Warszawa, Poland*

We study Friedel oscillations and screening effects of the impurity potential in the Hubbard model. Electronic correlations are accounted for by solving the real-space dynamical mean-field theory equations using the continuous-time quantum Monte Carlo simulations at finite temperatures and using a homogeneous self-energy approximation with the numerical renormalization group at zero temperature. We find that in the Fermi-liquid phase both the amplitudes of Friedel oscillations and the screening charge decrease with increasing the interaction and follow the behavior of the Fermi-liquid renormalization factor. Inside the Mott insulator regime, the Friedel oscillations are absent but the residual screening charge remains finite.

I. INTRODUCTION

The Friedel oscillation (FO) is a quantum mechanical phenomenon observed in metals in presence of an inhomogeneous, space-dependent potential [1–4]. FOs are seen in such physical properties as a charge density or a local density of states at a given energy. For example, if either an ion or a defect is inserted into a metal, breaking a translational invariance, then the electrons with energies near the Fermi surface are scattered yielding spatial oscillations in the charge density surrounding the inhomogeneity. This effect survives even at finite temperatures T as long as $T/T_F \ll 1$, where T_F is the Fermi temperature. FOs can be viewed as a quantum analog of classical screening of a charged impurity in a plasma. However, in the classical case the change in the charge density decays exponentially with a distance from the impurity and without oscillations. In the quantum regime the decay is polynomial with a rippling pattern formed by alternating regions of higher and lower electronic densities. The charge density $\bar{n}(r)$ very far from the impurity in a noninteracting, continuous system is given by

$$\bar{n}(r) = \bar{n}_{\text{hom}} + A\frac{\cos(2k_F r + \delta)}{r^d}, \qquad (1)$$

where $\bar{n}_{\text{hom}}$ is the uniform density, A is the amplitude of the FO, δ is a phase shift, and d is the dimension of the system [1–4]. The formula (1) is valid in the asymptotic limit with $k_F r \gg 1$, where k_F is the Fermi momentum and r is a distance from the impurity.

FOs were predicted by Friedel in a series of papers [1,2] and then became an essential component in the study of metallic alloys; for reviews see [5–8]. The first direct observations of FOs [9–12] were possible after invention of the scanning tunneling microscopy (STM) [13]. In fact, signatures of FOs were experimentally seen in various metals and semiconductors, for example, on surfaces Cu(111), GaAs(111), or Si(111)Ag [9,14,15]. In recent years observation of FOs reveals interesting features in solids, such as direction-dependent giant charge oscillations on ferromagnetic Fe film grown on W(001) surface [16] or an interaction-induced band with a well-defined dispersion existing in addition to conventional surface-state bands at noble metal surfaces [17]. STM studies have further shown that FOs induce asymmetry in the electron transport at the monolayer-bilayer interfaces in epitaxial graphene on SiC (001) which may find future application in quantum switching [18].

After the initial prediction [1,2], further theoretical investigations were performed to understand FOs in crystals with nonspherical Fermi surfaces [19–26], in model systems with an impurity on which the electrons can interact [27–31], in one-dimensional quantum wires where interacting electrons form a Luttinger liquid [32–38], in two- or three-dimensional Hubbard models with electrons forming either the Fermi liquid or the Mott insulator [39–44], or in system with interacting and disordered electrons such as amorphous alloys and quasicrystals [45]. Recent theoretical progress was made in understanding spin-dependent FOs [46], as well as understanding FOs in topological insulators [47,48], in graphane [49–51], in cold atoms [52], in systems with charge density waves [53], or with presence of the transport currents [54]. It was also noted that FOs can be used as a probing tool of quasiparticles [55]. Additionally, FOs lead to an effective interaction between localized magnetic moments which is mediated by conducting electrons and is known as the Ruderman-Kittel-Kasuya-Yosida (RKKY) interaction [56–59]. A related issue to the FOs is the Friedel sum rule which holds for both noninteracting [1,2,22,25] as well as for interacting electrons [60–63].

*byczuk@fuw.edu.pl

Different studies of FOs in Fermi liquids revealed that the oscillations are renormalized due to the electronic interactions. Although the charge FOs in the Hubbard model and the spin liquid at the Mott transition were studied [39–44], a comprehensive quantitative analysis of the FOs at the Mott transition is still an open problem. In particular, we would like to address quantitatively the following questions: How does the oscillation amplitude A change with the interaction strength? How does it behave at the Mott transition? What is a relation between the Fermi-liquid renormalization factor and the amplitude A? These problems are particularly interesting in the context of transition metal oxides. It motivated us to study the FOs in a model system of interacting lattice fermions within the real-space dynamical mean-field theory (R-DMFT) [40,64–69].

The R-DMFT is a reliable, self-consistent, and comprehensive approximation for interacting lattice fermions describing both the Fermi liquid as well the Mott insulator [70,71]. In this paper we show the disappearance of the FO at the Mott transition for the finite lattice systems.

The paper is organized as follows: In Sec. II we describe our model. In Sec. III we introduce R-DMFT formalism, discuss methods to solve it in different temperature regimes, and define interesting physical quantities. In Secs. IV and V we present numerical results for FOs as well as discuss and explain physical properties of the system. In Sec. VI we present conclusions and an outlook for possible future investigation including a discussion on observing signatures of FOs in real materials with correlated electrons and raise the question if FOs would influence the charge transport properties in such materials.

II. MODEL

We study FOs within a one-band Hubbard model in presence of an external impurity potential and given by the Hamiltonian

$$H = \sum_{ij\sigma} t_{ij}\, \hat{a}^\dagger_{i\sigma}\, \hat{a}_{j\sigma} + \sum_{i\sigma} V_{i\sigma}\, \hat{a}^\dagger_{i\sigma}\, \hat{a}_{i\sigma} + U \sum_i \hat{n}_{i\downarrow}\hat{n}_{i\uparrow}, \quad (2)$$

where $\hat{a}_{i\sigma}$ ($\hat{a}^\dagger_{i\sigma}$) is the annihilation (creation) fermionic operator with spin σ on the ith lattice site, t_{ij} is the hopping matrix element between the ith and jth sites with $t_{ii} = 0$. The second term describes the external (inhomogeneous) potential energy $V_{i\sigma}$. The third term models the interaction energy when two fermions with opposite spins are located on the same lattice site.

In this paper we consider a local impurity potential $V_i = V_0\, \delta_{i,i_0}$, where i_0 represents the lattice site $\vec{R}_{i_0}$. We study finite lattice systems on a two-dimensional (2D) square lattice and on a three-dimensional (3D) cubic lattice. We consider paramagnetic systems without any long-range order and apply a periodic boundary condition. The Hamiltonian (2) is solved within R-DMFT approximation [40,65–69].

III. R-DMFT FORMALISM AND PHYSICAL QUANTITIES

A. Matsubara Green's functions

All physical properties, which are studied here, are obtained from one-particle Green's functions defined

by

$$G_{ij\sigma}(\tau) = -\langle T_\tau \hat{a}_{i\sigma}(\tau)\hat{a}^\dagger_{j\sigma}(0)\rangle, \quad (3)$$

where $\tau \in (0, \beta)$ is the imaginary time and $\beta = 1/T$ denotes the inverse temperature with the Boltzmann constant equal to unity [72]. The symbol T_τ means the chronological operator and $\langle \dots \rangle$ represents both quantum and thermal averages in the grand-canonical ensemble with a fixed chemical potential μ. Later we also perform Fourier transformation to obtain the Green's functions $G_{ij\sigma}(i\omega_n)$, where $\omega_n = (2n + 1)\pi/\beta$ are fermionic Matsubara frequencies with integer n.

B. R-DMFT

The Green's functions (3) in Matsubara frequency space obey an exact Dyson equation

$$G_{ij\sigma}(i\omega_n) = G^{(0)}_{ij\sigma}(i\omega_n) + \sum_{kl} G^{(0)}_{ik\sigma}(i\omega_n)\Sigma_{kl\sigma}G_{lj\sigma}(i\omega_n), \quad (4)$$

where $G^{(0)}_{ij\sigma}(i\omega_n)$ are the Green's functions at $U = 0$. The self-energies $\Sigma_{kl\sigma}(i\omega_n)$ account for all interaction effects. The main approximation of R-DMFT [70] is that the self-energies are local, which means that they are diagonal in the lattice site indices, i.e.,

$$\Sigma_{ij\sigma}(i\omega_n) = \Sigma_{i\sigma}(i\omega_n)\delta_{ij}, \quad (5)$$

where δ_{ij} is the Kronecker delta. Nevertheless, they are site dependent for inhomogeneous systems [40,65–69].

R-DMFT approximation consists of the following set of self-consistent equations: At each lattice site l the reduced partition function, obtained within the cavity method [71], is given by

$$Z^l = \int D[a_{l\sigma}, a^*_{l\sigma}]e^{-S_l[a_{l\sigma}, a^*_{l\sigma}]}, \quad (6)$$

where the local action S^l is

$$S_l = -\int_0^\beta d\tau_1 \int_0^\beta d\tau_2 \sum_\sigma a^*_{l\sigma}(\tau_1)\mathcal{G}^{-1}_{l\sigma}(\tau_1 - \tau_2)a_{l\sigma}(\tau_2)$$
$$+ U\int_0^\beta d\tau\, a^*_{l\uparrow}(\tau)a_{l\uparrow}(\tau)a^*_{l\downarrow}(\tau)a_{l\downarrow}(\tau). \quad (7)$$

In Eq. (7) the path-integral formalism in the coherent state representation is used with $a^*_{l\sigma}$ and $a_{l\sigma}$ as Grassmann variables [72]. In Eq. (7) the kernel

$$\mathcal{G}^{-1}_{l\sigma}(\tau_1 - \tau_2) \equiv -\left(\frac{\partial}{\partial \tau_1} - \mu + V_l\right)\delta(\tau_1 - \tau_2) - \Delta_{l\sigma}(\tau_1 - \tau_2)$$
$$(8)$$

is the inverse of the mean-field propagator and

$$\Delta_{l\sigma}(\tau_1 - \tau_2) \equiv -\sum_{ij} t_{li}G^l_{ij\sigma}(\tau_1 - \tau_2)t_{jl} \quad (9)$$

is the hybridization function, which physically accounts for the coupling of the lth site with the rest of the lattice. $G^l_{ij\sigma}(\tau)$ is the Green's function on a lattice with a cavity on site l. The symbol $\delta(\tau)$ represents the Dirac function. The mean-field

propagators $\mathcal{G}_{l\sigma}(i\omega_n)$ are related to the diagonal matrix elements $[\mathbf{G}_\sigma(i\omega_n)]_{ll}$ of the one-particle matrix Green's function by the local Dyson equation

$$\mathcal{G}_{l\sigma}^{-1}(i\omega_n) = [\mathbf{\Sigma}_\sigma(i\omega_n)]_{ll} + \frac{1}{[\mathbf{G}_\sigma(i\omega_n)]_{ll}}. \qquad (10)$$

We use notation where the matrices are given by $[\mathbf{G}_\sigma(i\omega_n)]_{ij} = G_{ij\sigma}(i\omega_n)$ and $[\mathbf{\Sigma}_\sigma(i\omega_n)]_{ij} = \Sigma_{ij\sigma}(i\omega_n)$, respectively. The lattice Green's functions are obtained by inverting the real-space Dyson equations (4), which in a matrix form read as

$$\mathbf{G}_\sigma(i\omega_n) = [\xi(i\omega_n) - \mathbf{t} - \mathbf{\Sigma}_\sigma(i\omega_n)]^{-1}, \qquad (11)$$

where $[\xi(i\omega_n)]_{ij} = (i\omega_n + \mu - V_i)\delta_{ij}$. The hopping matrix is given by $[\mathbf{t}]_{ij} = t_{ij}$ and the matrix self-energy is obtained within the local approximation (5). Finally, the functional integrals determining the diagonal matrix elements of the Green's functions are given by

$$[\mathbf{G}_\sigma(i\omega_n)]_{ll} = -\frac{1}{Z^l} \int \prod_\sigma D[a_{l\sigma}^*, a_{l\sigma}][a_{l\sigma}(i\omega_n)a_{l\sigma}^*(i\omega_n)]$$
$$\times e^{-S_l[a_{l\sigma}^*, a_{l\sigma}]}. \qquad (12)$$

The set of Eqs. (4)–(12) constitutes R-DMFT and those equations are solved numerically in an iterative way.

C. R-DMFT within CT-QMC

Among different R-DMFT self-consistency equations (4)–(12) the most difficult is to solve the problem in Eq. (12). Here, we solve it by using continuous-time quantum Monte Carlo (CT-QMC) simulations, where the partition function is expanded about the hybridization function and resummed by using a stochastic Metropolis algorithm [73]. The computer program developed by us is based on the approach of Haule [74]. In this method the problem is solved in the Matsubara frequency space. CT-QMC only works for finite temperatures and the computational timescales at least linearly with β. In this method the problem (12) is solved on every nonequivalent lattice site. These factors made that the solution of R-DMFT within CT-QMC very time consuming, in particular, at low temperatures and for large lattice systems in higher dimensions (e.g., 3D), exactly where DMFT approximation is supposed to be more accurate.

D. R-DMFT within homogeneous self-energy approximation

Due to these limitations of CT-QMC we also use an approximate method to solve R-DMFT equations, which is described now. The self-energy $\Sigma_{i\sigma}(i\omega_n)$ in Eq. (4) can be split into a homogeneous and an inhomogeneous part as follows:

$$\Sigma_{i\sigma}(i\omega_n) = \Sigma_\sigma(i\omega_n) + \Delta\Sigma_{i\sigma}(i\omega_n). \qquad (13)$$

The first term accounts for the interaction effects in a homogeneous system and it is therefore site independent. We want to describe FOs very far from the impurity, i.e., at sites $\vec{R}_i$ such that $|\vec{R}_i - \vec{R}_{i_0}| \gg a$, where a is a lattice constant, and make a contact with the original formula (1). Therefore, since far away from the impurity the effect of $V_{i\sigma}$ on the self-energy is expected to be weak, the inhomogeneous part

$\Delta\Sigma_{i\sigma}(i\omega_n)$ can be neglected. The homogeneous part $\Sigma_\sigma(\omega) = \Sigma_\sigma(i\omega_n \longrightarrow \omega + i0^+)$ is determined by solving the dynamical mean-field theory (DMFT) self-consistency equations for infinite homogeneous system [71] at zero temperature by using the numerical renormalization group (NRG) method [75]. The open-source code NRG LJUBLJANA is used for that purpose [76]. The computed self-energy is then transferred into the real-space Dyson equation (11) containing the impurity potential V_i in order to obtain the Green's function. This approach to solving R-DMFT is called the homogeneous self-energy approximation (HSEA). Within HSEA we could perform a complete analysis of the 2D systems and some preliminary studies of 3D systems.

We note that HSEA is not equivalent to the commonly used local density approximation (LDA), e.g., [68], and only the former gives rise to FOs. The LDA, also known as a Thomas-Fermi or WKB approximation, corresponds to the replacement of k-integrated Dyson equation in the homogeneous DMFT [71] by $G_{ii\sigma}(\omega) = \sum_{\vec{k}} 1/[\omega - \epsilon_{\vec{k}} - V_i - \Sigma(\omega)]$, where $\epsilon_{\vec{k}}$ is a noninteracting dispersion relation in momentum $\vec{k}$ space. Within HSEA the real-space Dyson equation (4), after Fourier transformation, takes the form $G_{ii\sigma}(\omega) = \sum_{\vec{k}\vec{k}'} e^{i\vec{R}_i(\vec{k}-\vec{k}')} G_{\vec{k}\vec{k}'}(\omega)$, where $G_{\vec{k}\vec{k}'}(\omega) = [\mathbf{G}^0(\omega)^{-1} - \Sigma(\omega)\mathbf{1}]_{\vec{k}\vec{k}'}^{-1}$, with $[\mathbf{1}]_{\vec{k}\vec{k}'} = \delta_{\vec{k}\vec{k}'}$, $[\mathbf{G}^0(\omega)^{-1}]_{\vec{k}\vec{k}'} = (\omega - \epsilon_{\vec{k}})\delta_{\vec{k}\vec{k}'} - V_{\vec{k}\vec{k}'}$, and $V_{\vec{k}\vec{k}'}$ being a Fourier transform of the potential V_i. The presence of oscillatory terms with $\vec{k} \neq \vec{k}'$ yields FOs.

E. Physical quantities

The most desired physical quantity in studying the FOs is the average number of particles on each lattice site $\bar{n}_{i\sigma} \equiv \langle \hat{a}_{i\sigma}^\dagger \hat{a}_{i\sigma} \rangle$, i.e., the spin-resolved particle density. In case of R-DMFT solved within CT-QMC the spin-resolved density of particles, given by

$$\bar{n}_{i\sigma} = \lim_{\tau \to 0^-} G_{ii\sigma}(\tau), \qquad (14)$$

is directly determined from the Monte Carlo simulations. Since this method is based on stochastic sampling, the statistical error given by the standard deviation of different samples is also estimated here.

In case of HSEA we determine the retarded one-particle Green's function [72] and then we find the local spectral function

$$A_{i\sigma}(\omega) = -\frac{1}{\pi} \text{Im } G_{ii\sigma}(\omega). \qquad (15)$$

Having $A_{i\sigma}(\omega)$ we compute the spin-resolved particle density at finite temperatures according to

$$\bar{n}_{i\sigma} = \int_{-\infty}^{+\infty} A_{i\sigma}(\omega) f(\omega) \, d\omega, \qquad (16)$$

where $f(\omega)$ is the Fermi-Dirac distribution function.

The total number of particles per site is given by

$$\bar{n} = \frac{1}{N_L} \sum_{i=1}^{N_L} \bar{n}_i, \qquad (17)$$

where $\bar{n}_i = \bar{n}_{i\uparrow} + \bar{n}_{i\downarrow}$ and N_L is the number of the lattice sites. Since in this paper we consider spin-rotationally invariant systems, the equality $\bar{n}_{i\uparrow} = \bar{n}_{i\downarrow}$ holds.

The screening effect, i.e., a shielding of the impurity potential by the conducting electrons [3], is quantified by the so-called screening charge according to

$$Z = \sum_i (\bar{n}_i - \bar{n}_{hom}), \qquad (18)$$

where the summation runs over all lattice sites and $\bar{n}_{hom}$ corresponds to the particle density of the corresponding homogeneous system with $V_i = 0$.

IV. NUMERICAL RESULTS FOR R-DMFT WITHIN CT-QMC

In this section we present numerical results obtained within CT-QMC solver for R-DMFT equations. In the following, we choose the chemical potential $\mu = U/2$ so that the homogeneous system is at half-filling with the density $\bar{n} = 1$. We consider finite lattice systems. In all cases the hopping amplitude $t_{ij} = t$ is only between nearest neighbors. We set $t = 1$ to define the energy unit and the lattice constant $a = 1$ to define the length unit. The bandwidth W is given by $W = 2zt$, where z is the coordination number. The system is subjected to periodic boundary conditions with a finite number N_L of the lattice sites.

A. Two-dimensional square lattice

We first present our results for a two-dimensional square lattice for a system size of 31×31. In case of R-DMFT within CT-QMC we perform simulations for finite temperatures corresponding to $\beta = 5/t$ and $15/t$. These temperatures are within the crossover regime of the U-T phase diagram, above the critical temperature for the square lattice [77]. In Figs. 1 and 2 the FOs are shown for the above-mentioned lattice with the impurity $V_0 = 6t$ placed in the center at $\vec{R}_0 = (16a, 16a)$. In Fig. 1 we present results at $\beta = 5/t$ and in Fig. 2 at $\beta = 15/t$ for $U = t, 5t, 8t$ in each case. It is clearly seen that with increasing the interaction the FO amplitudes diminish and almost no oscillation is seen for $U = 8t$ for both temperatures. We note that the linearized DMFT predicts $U_c = 6\sqrt{z}t \approx 12t$ at $T = 0$ and $z = 2d = 4$ [78]. At finite T, U_c is smaller and $U = 8t$ may already mark an approximate Mott transition point. Hence, we report the disappearance of FOs on approaching the Mott transition in this case. We further note that FOs are stronger, i.e., more visible, at lower temperatures (cf. Figs. 1 and 2). FO decays as $1/r^2$ in two dimensions.

The stochastic nature of the CT-QMC and resulting numerical inaccuracy make it impossible to provide more detailed analysis of the FOs decays. Improving the numerical accuracy of our simulations, in particular, to get results for the FOs in three-dimensional systems is beyond our current CT-QMC implementation (see Appendix B for technical details). Therefore, in the next section we revert to the Hubbard model on a one-dimensional (1D) lattice to gain more insights about the decay of the FOs and the behavior of the screening charge at
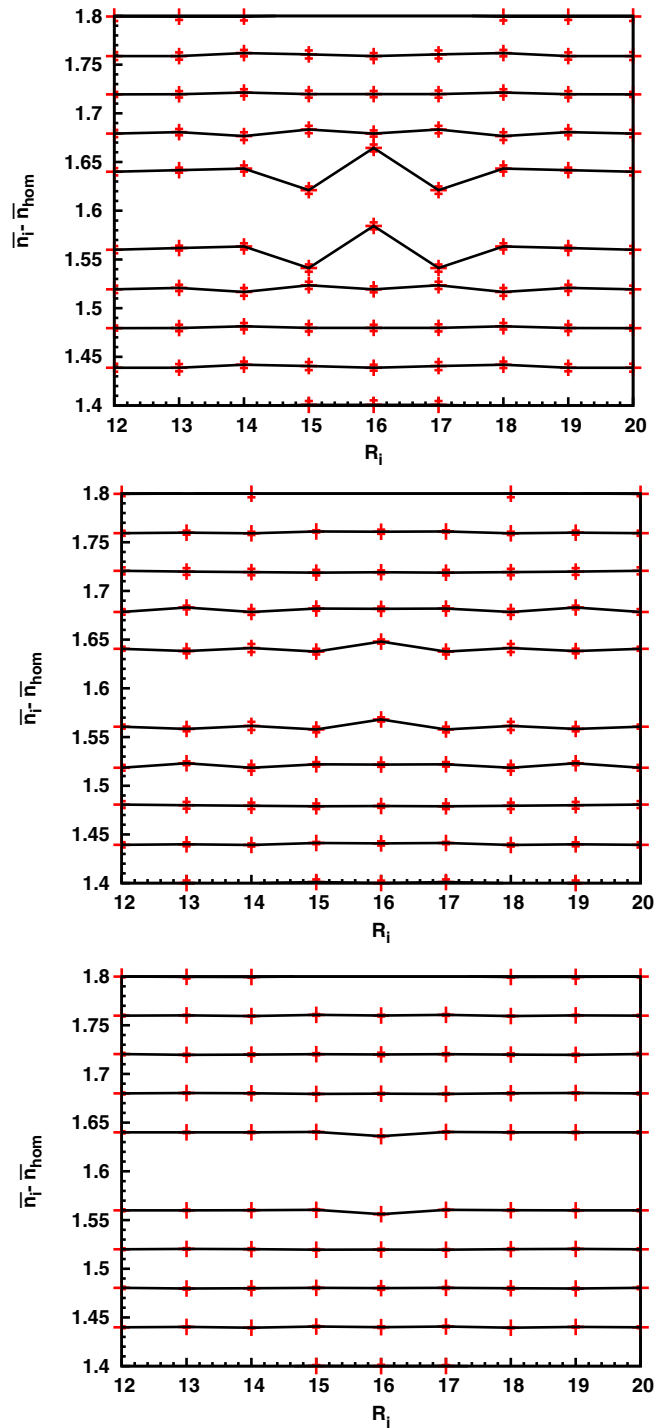

FIG. 1. Friedel oscillations in particle densities of the Hubbard model in two-dimensional square lattice with 31×31 sites. The impurity potential $V_0 = 6t$ is located in the center at $\mathbf{R}_0 = (16a, 16a)$ and the temperature is set to $\beta = 5/t$. Densities variations $\bar{n}_i - \bar{n}_{hom}$ are plotted along the horizontal (x) axis for different sections in the vertical (y) direction of the lattice. The distance between ticks on the vertical axis is 0.02. The line with the impurity potential is excluded. In the upper, middle, and lower panels the interaction is $U = t, 5t$, and $8t$, respectively. Stochastic error bars are shown.
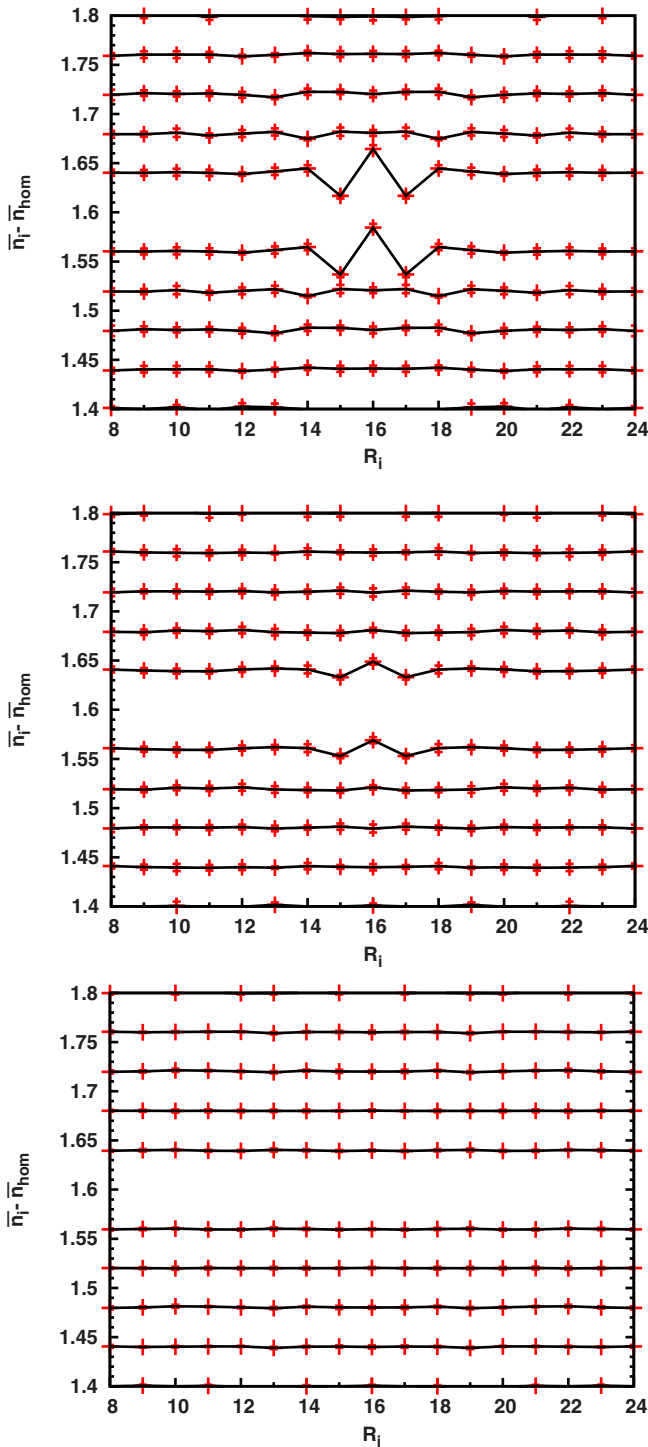
FIG. 2. Friedel oscillations in particle densities of the Hubbard model with the temperature $\beta = 15/t$ in two-dimensional square lattice. The other parameters and style of plotting are the same as in Fig. 1.

finite interactions and nonzero temperatures from a toy model, as explained below.

B. One-dimensional chain

According to the exact Bethe ansatz solution of the Hubbard model on 1D lattice with half-filling there is a Mott

insulating state for any finite interaction [79]. Moreover, away from half-filling the Fermi-liquid picture breaks down and the electrons are in a Luttinger-liquid state. On the other hand, the DMFT provides an exact solution of the Hubbard model in the infinite dimensions [70]. At finite dimensions, DMFT approximates the self-energy by the momentum-independent one and, therefore, reproduces features of the Fermi liquid even in one dimension. We make use of this artifact of DMFT to gain some insights about the FOs in higher-dimensional systems from studying the behavior of the 1D Hubbard model. We emphasize that we do not represent any real 1D system (e.g., a quantum wire) using our "toy model" but just use it as a computational trick to circumvent the limitations of simulating higher-dimensional systems within R-DMFT+CT-QMC.

We first study the "theoretical Mott transition" for a one-dimensional homogeneous Hubbard model ("toy model") at finite temperature in order to estimate the critical temperature and interactions for such systems. We use the method of discontinuity in the double occupancy with the interactions in order to obtain these estimates (see Appendix A, [80]). According to our results, for $\beta = 20/t$ the coexistence region exits between the metallic and insulating phases with the two transition points $U_{c1} = 6.6t$, $U_{c2} = 7.2t$. Similar to the case of 2D, here the critical interaction is slightly less than the predicted value from the linearized DMFT ($U_c = 6\sqrt{z}t \approx 8.5t$ at $T = 0$) due to the finite-temperature effects (see Appendix C, [78]).

Here we consider a one-dimensional lattice chain with the number of lattice sites $N_L = 50$. We perform simulations for finite temperatures corresponding to $\beta = 5/t$ and $20/t$.

In Fig. 3 we present the density $\bar{n}_i$ on different lattice sites with the impurity potential $V_0 = 2t$ set on $|\vec{R}_i| = 5a$ site. The upper panel shows FO at $\beta = 5/t$ and the lower panel shows FO at $\beta = 20/t$. Results are presented for different interactions U marked by lines in different colors. In the zoomed areas we show FO in the vicinity of the impurity site. Away from the impurity site the relative changes in the densities are very small, much lower than 1%. The amplitudes of FO are larger than the 2D due to a slower $1/r$ decay in this case and hence easier to visualize. Similar to 2D, the oscillations are more pronounced at lower temperatures and damped with the increasing interactions. We note that the period and the phase shift of the oscillations remain unchanged and stay the same at different temperatures. With the help of Eq. (1) it means that at half-filling the length of the Fermi wave vector k_F and the phase shift are invariant with respect to the interaction change. However, this is not the case away from the half-filling where the particle-hole symmetry breaks. Although the Fermi volume, i.e., the length of k_F in 1D, is invariant according to the Luttinger theorem, the phase shift of FO changes with the interaction.

In the case of 1D systems at half-filling we could perform a more quantitative analysis to understand the decay of the FO amplitudes with the increasing interaction. In Fig. 4 we plot the local density deviations $|\bar{n}_i - \bar{n}_{\text{hom}}|$ as a function of the inverse of the relative distance from the impurity site, i.e., $1/|\vec{R}_i - \vec{R}_{i_0}|$. The asymptotic linear decay is visible in agreement with Eq. (1) in the presence of interactions for both the temperatures. In case of $\beta = 5/t$ we see more random
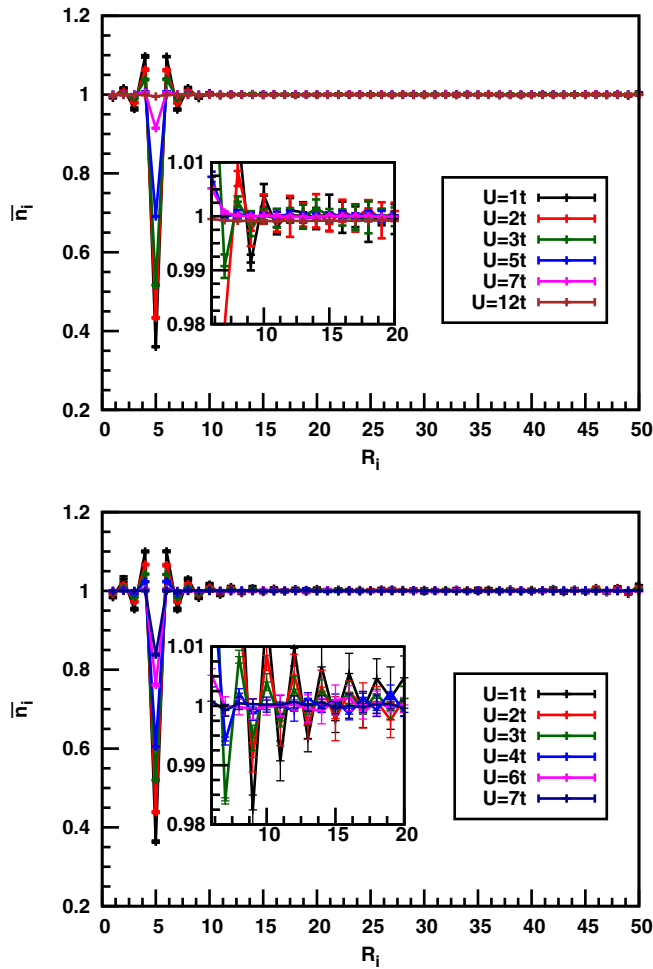
FIG. 3. Friedel oscillations in particle densities at different lattice site in presence of the single impurity potential $V_0 = 2t$ placed at $|\vec{R}_i| = 5a$ in a 1D chain with $N_L = 50$ sites. Upper (lower) panel presents results for $\beta = 5/t$ ($\beta = 20/t$). Different colors correspond to different interactions U which are accounted for by using R-DMFT within CT-QMC. Corresponding stochastic error bars are also shown. The insets show FOs in the neighborhood of the impurity.
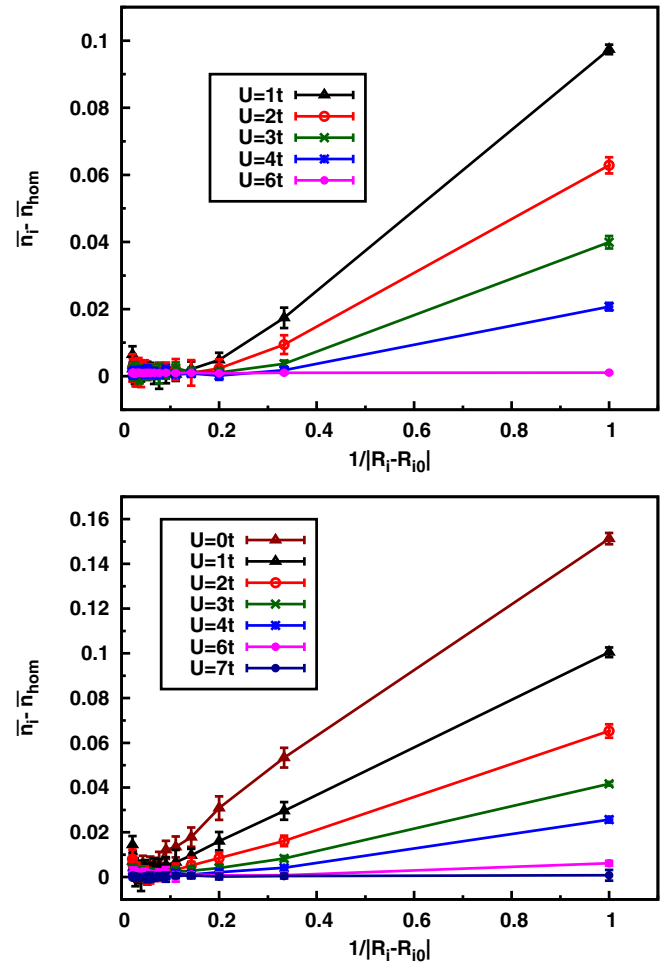

FIG. 4. Variation of the density deviations as a function of inverse of the relative distance from the impurity site for the same system and method as in Fig. 3. In the upper (lower) panel we show results for $\beta = 5/t$ ($\beta = 20/t$).

deviations in the maxima of the local density as compared to $\beta = 20/t$. This is due to a smallness of the FO amplitudes in the former case and stochastic nature of the CT-QMC results. The points shown in Fig. 4 follow the approximate linear rule $|\bar{n}_i - \bar{n}_{\mathrm{hom}}| = Ax + B$, where $x = 1/|\vec{R}_i - \vec{R}_{i_0}|$. The parameters A and B can be determined by fitting procedure. Of particular interest is the slope parameter $A = A(U)$ which describes changes in the FO amplitude with U. We perform a linear fit for the case of $\beta = 20/t$ and present it in Fig. 5. We see that the slope $A(U)$ decreases with increasing U and vanishes at $U \approx 7t$ which lies within our numerically obtained value of the transition points $U_{c1} = 6.6t$ and $U_{c2} = 7.2t$ (cf. Fig. 6). Thus, in this case we report the disappearance of FO at the Mott transition (see Appendix B for details).

The screening charge Z, defined in Eq. (18), is shown in Fig. 7. Since the impurity potential is repulsive $V_0 = 2t > 0$ the particles are pushed away ($Z < 0$) from the system which is treated within the grand canonical ensemble with a constant chemical potential $\mu = U/2$ as discussed at the beginning.
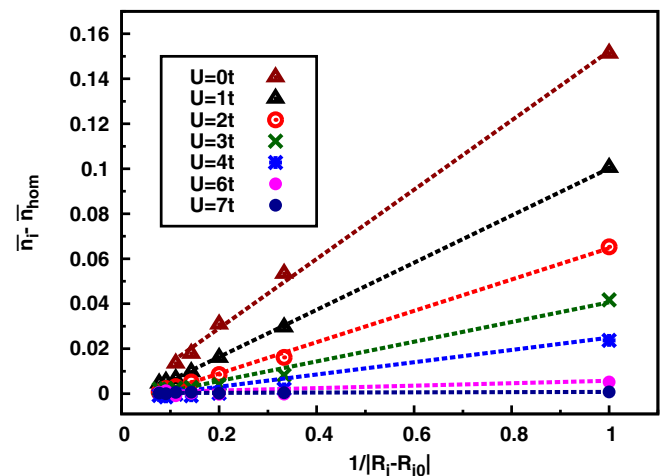

FIG. 5. Linear fits for points in Fig. 4 in the lower panel for $\beta = 20/t$. The slope $A(U)$ decreases with increasing U and vanishes on the insulating side.
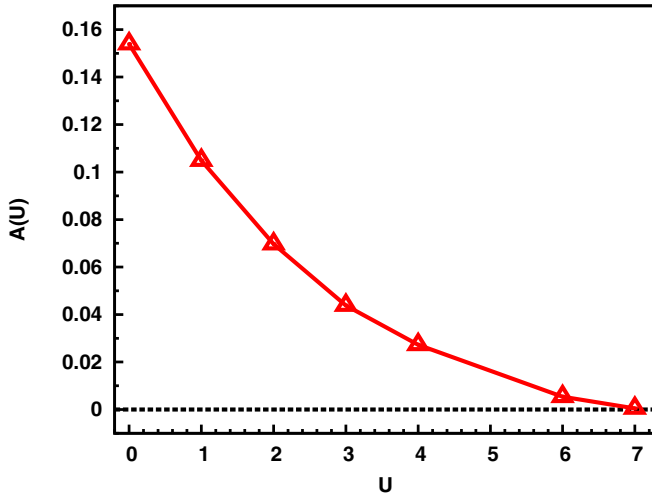
FIG. 6. Variation of the relative slope $A(U)/A(0)$ determined from Fig. 5 for $\beta = 20/t$ as a function of U with $A(0) = 0.154$.

With increasing the interaction the screening of the impurity is weaker, i.e., the number of removed charge is smaller, as is seen in the upper panel of Fig. 7.

When the system turns into a Mott phase with a correlation gap, the screening is ineffective and Z approaches zero as shown in the upper panel of Fig. 7. We find rather weak dependence of the screening charge on the temperature, which is illustrated in the lower panel of Fig. 7. The insights provided by studying our 1D "toy model" need further investigations using higher-dimensional lattice systems with a large number of lattice sites.

We could not achieve lower temperatures, higher dimensions, and precise numerical accuracy in our calculations using the R-DMFT+CT-QMC method (see Appendix B). Therefore, we turn to HSEA approach for the further studies of FOs in the Hubbard model. Using this approach we could perform simulations at $T = 0$ (strictly speaking at $\beta = 10\,000/t$), we could study higher-dimensional lattices, i.e., 2D and 3D systems where DMFT is a more accurate method. In Appendix C we explicitly compare HSEA with the exact results of CT-QMC for the 1D toy model and show a good qualitative agreement in the behavior of the FO's decay, screening charge with the interactions obtained from the two methods. We could also compare the results of our 1D "toy model" with the higher-dimensional models finding the expected similarities. We thus claim the HSEA to be a reliable approximation also for the higher-dimensional systems. Particularly, our initial results on 3D systems are a good starting point to gain knowledge about the behavior of the FOs in real materials where effects of electronic correlations are significant.

V. NUMERICAL RESULTS FOR R-DMFT WITHIN HSEA

In this section we present our numerical results obtained within HSEA. We determine the DMFT self-energy for a given U by using the NRG at zero temperature. This self-energy is inserted into the Dyson equation (4) to obtain the Green's functions and other physical quantities, as discussed
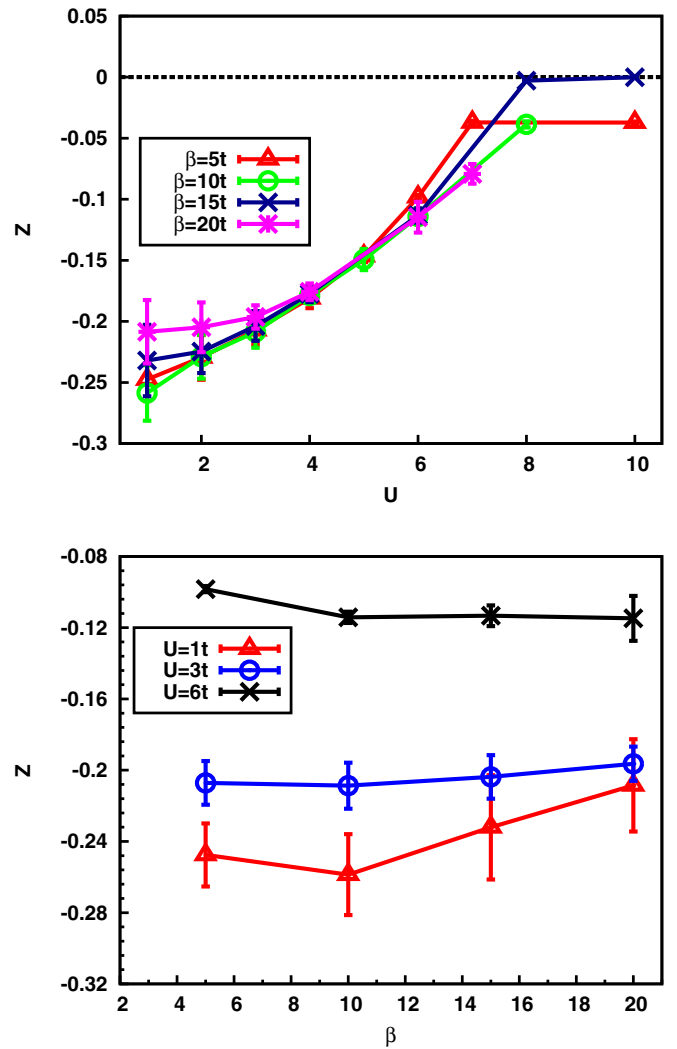

FIG. 7. Screening charge Z determined from Eq. (18) as a function of interaction U (upper panel) and temperature (lower panel). The system parameters are the same as in Fig. 3.

in Sec. III. Since we start from using the NRG self-energies, the Green's functions are determined on the real-frequency axis. As in the former section, the chemical potential is fixed at $\mu = U/2$ to keep the homogeneous systems at half-filling with $\bar{n} = 1$. Within the HSEA we are able to work within much larger lattices in higher dimensions as compared to the previous case of CT-QMC. Hence, we consider a square lattice and a cubic lattice here. In both cases, the hopping amplitude $t_{ij} = t$ is only between nearest neighbors and $t = 1$ as earlier.

A. Two-dimensional square lattices

The FOs in the two-dimensional lattice with the HSEA are presented in Figs. 8 and 9. The lattice size is 31×31 and the impurity potential $V_0 = 24t$ is located in the center. The main panels of Figs. 8 and 9 show two-dimensional color maps of FOs seen in the particle density. In the insets the FOs are shown along the vertical line crossing the impurity site. The FOs are not spherically symmetric as in a free space but possess the square-lattice symmetry. Due to constructive
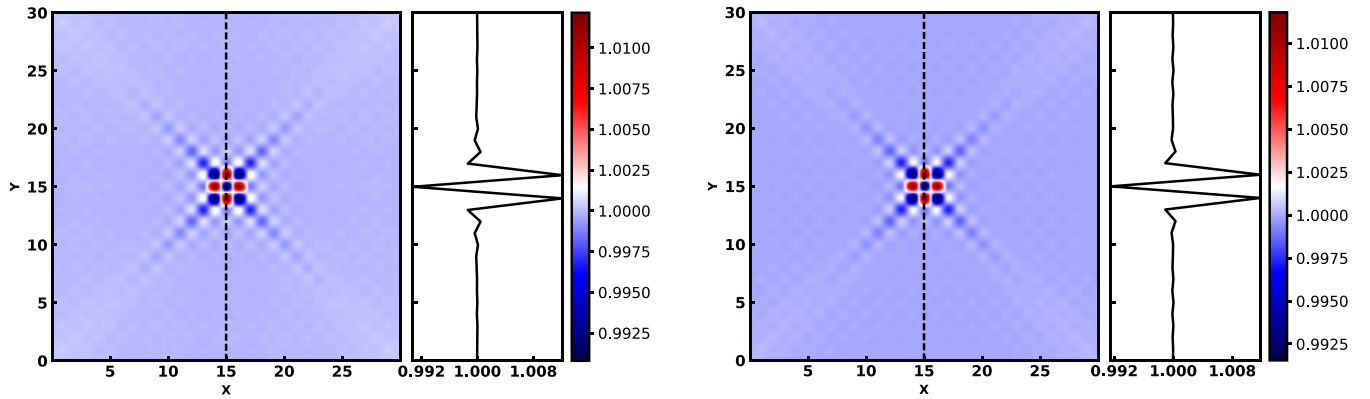
FIG. 8. Friedel oscillations in particle densities of the Hubbard model in two-dimensional square lattice with 31×31 sites. The impurity potential $V_0 = 24t$ is located in the center at $\vec{R}_0 = (15a, 15a)$ and the interaction $U = 0$ (left panel) and $2t$ (right panel). The insets show FOs along vertical line crossing the impurity site. The color scale is spanned in-between the highest and lowest values of density in the system. The color scale changes for different U's since the minimal value of the density increases with U as shown in the insets.

interference of oscillatory waves along horizontal and vertical directions the strongest FOs are observed along these lines. The amplitudes of FOs are much smaller as compared to those in one-dimensional cases because of the damping factor $1/r^2$. It is also clearly seen that by increasing the interaction the amplitudes of the oscillations are weaker and as the system becomes an insulator the FOs far from the impurity are absent. In insulator there are still visible deviations in the density of particles in the neighborhood of the impurity site. We do not show the densities on the impurity site but substituted them by the second smallest value in the plots. Otherwise, the impurity contribution would overshadow any oscillations in $\bar{n}_i$ due to their fast power-law decay with a distance.

In Fig. 10 we plot the local density deviations $|\bar{n}_i - \bar{n}_{\text{hom}}|$ as a function of the square of the inverse of the relative distance from the impurity site, i.e., $1/|\vec{R}_i - \vec{R}_{i_0}|^2$ for the densities shown in Figs. 8 and 9. Here, we show results along a line parallel to the diagonal one and shifted by one lattice constant. The $1/r^2$ decay in amplitude is visible in agreement with Eq. (1) in the presence of interactions. The points shown in Fig. 10 follow the approximate quadratic rule $|\bar{n}_i - \bar{n}_{\text{hom}}| =$

$Ax^2 + B$, where $x = 1/|\vec{R}_i - \vec{R}_{i_0}|$ and the parameters A and B are determined by fitting procedure.

In particular, the slope parameter $A = A(U)$ describes changes in the FO amplitude with U. We see that the slope $A(U)$ decreases with increasing U and vanishes at the metal-insulator transition (cf. Fig. 11) at $U_c \approx 12t$. The critical value U_c determined from the $A(U)$ curve is in perfect agreement with the linearized DMFT [78]. The value is larger than that obtained within CT-QMC because now the temperature is zero (strictly speaking, $\beta = 10\,000/t$).

Since a metallic system described with DMFT is within the Fermi-liquid regime, we expect that it must be fully quantified by the Fermi-liquid renormalization parameter and by the lifetime of quasiparticles. Both quantities are obtained by expanding the local self-energy at low frequencies, in the following way:

$$\Sigma(\omega, U) \approx \alpha(U)\omega + i\gamma(U)\omega^2, \qquad (19)$$

where parameters $\alpha(U) = (\partial \operatorname{Re}\Sigma(\omega, U)/\partial \omega)|_{\omega=0}$ and $\gamma(U) = (\partial^2 \operatorname{Im}\Sigma(\omega, U)/\partial \omega^2)|_{\omega=0}$ are determined numerically from the given NRG self-energy. In Fig. 11
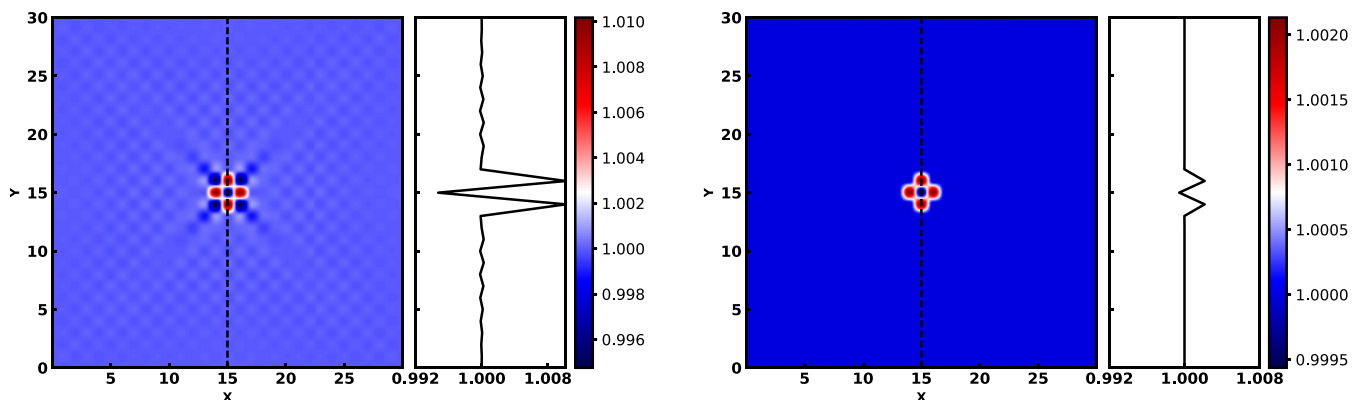

FIG. 9. Friedel oscillations in particle densities of the Hubbard model in two-dimensional square lattice with 31×31 sites. The impurity potential $V_0 = 24t$ is located in the center at $\vec{R}_0 = (15a, 15a)$ and the interaction $U = 5t$ (left panel) and $12t$ (right panel). The insets show FOs along vertical line crossing the impurity site and the color bars have the same legend as in Fig. 8.
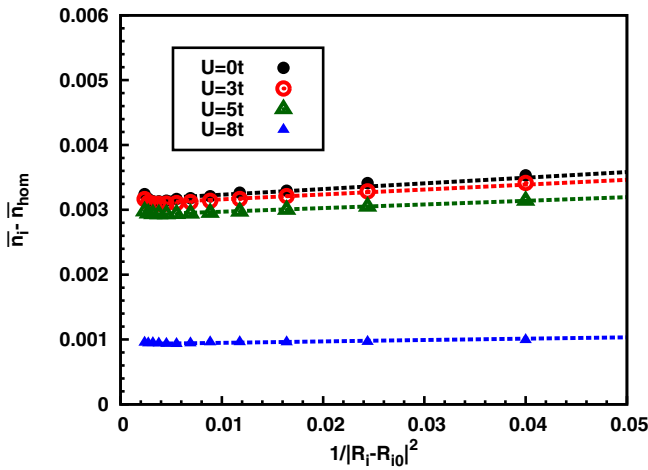
FIG. 10. Variation of the density deviations as a function of the square of inverse of the relative distance from the impurity site for the same system and method as in Figs. 8 and 9.

we plot both the Fermi-liquid renormalization factor $Z_{FL}(U) = 1/[1 - \alpha(U)]$ and the prefactor $\gamma(U)$ in the inverse of the quasiparticle lifetime for the Hubbard model in two dimensions. The renormalization factor $Z_{FL}(U)$ vanishes at the metal-insulator transition point U_c whereas the coefficient $\gamma(U)$ diverges there. We find that the FO amplitudes $A(U)$ follow the behavior of $Z_{FL}(U)$. This means that the renormalization of the quasiparticle wave functions is the primary source for damping of the FOs with increasing U. As expected, $Z_{FL}(U) = 0$ at U_c and FOs disappear.

As shown in [3] for the noninteracting systems, the particle density deviations away from the perturbing potential are given by $\Delta \bar{n}(r) = \lim_{R \to \infty} (R/\pi) \sum_{l=0}^{\infty} \int_0^{k_F} dk \int d\Omega [|\Psi_{kl}(r)|^2 - |\Psi_{kl}^0(r)|^2]$, where $\Psi_{kl}(r)$ and $\Psi_{kl}^0(r)$ are partial components of the wave
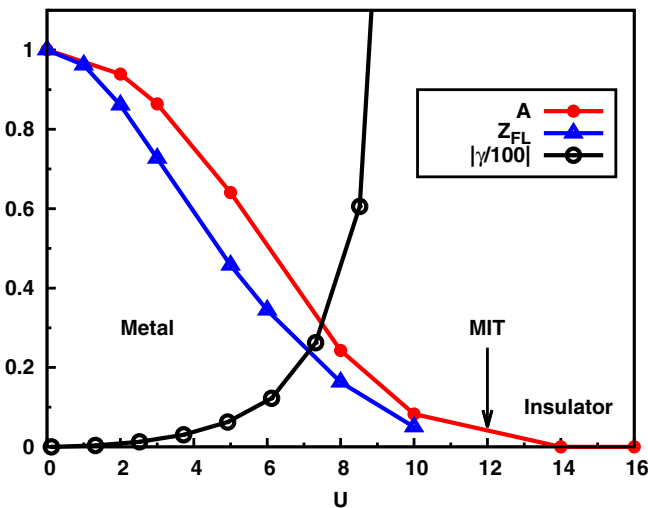

FIG. 11. Variations of the relative slope $A(U)/A(0)$ determined from Fig. 10 (red curve), the Fermi-liquid renormalization parameter (blue curve), and the inverse of quasiparticle lifetime (black curve) as functions of U and $A(0) = 0.009$.
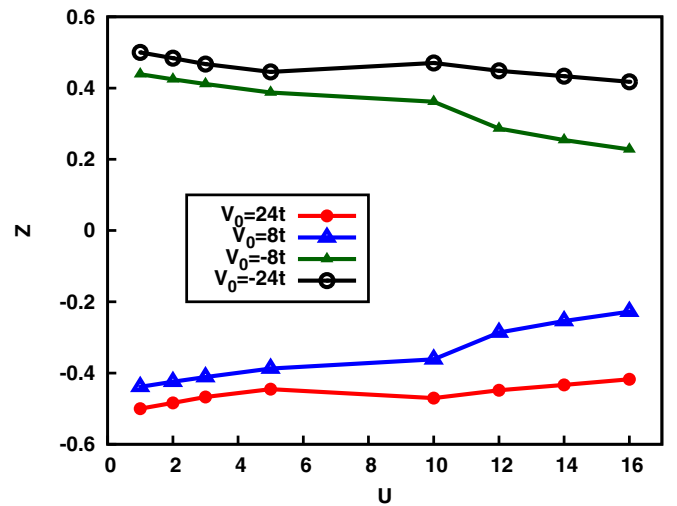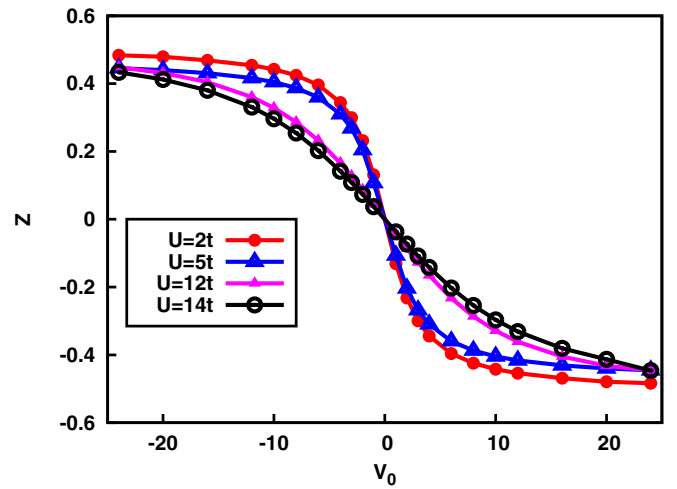

FIG. 12. Screening charge Z determined from Eq. (18) as a function of the impurity potential V_0 for selected U (upper panel) and as a function of the interaction U for $V_0 = \pm 8t$ and $\pm 24t$ (lower panel). The other system parameters are the same as in Fig. 8.

function in the spherical coordinates in the presence and the absence of the impurity, respectively. Taking into account the interaction effects in the Fermi-liquid picture, the wave functions of quasiparticles are renormalized (multiplied) by the square root of the renormalization factor $\sqrt{Z_{FL}(U)}$, i.e., $\Psi_{kl}^{quasi}(r) = \sqrt{Z_{FL}(U)} \Psi_{kl}(r)$. Thus, we expect that $\Delta \bar{n}(r) \sim Z_{FL}(U)$ in good agreement with our numerical findings.

The screening charge Z, defined in Eq. (18), is shown in Fig. 12. The repulsive $V_0 > 0$ potential leads to lowering the number of particles in the system whereas the attractive $V_0 < 0$ potential yields this number to increase. There is a perfect mirror symmetry between these two regimes as is seen in the upper panel in Fig. 12 for different U. With increasing the interaction, the screening of the impurity is weaker, i.e., the number of removed charges is smaller, as is presented in the upper and lower panels of Fig. 12. A change in the behavior of Z is seen around the Mott transition. Although the screening charge $|Z|$ is a decreasing function of U it
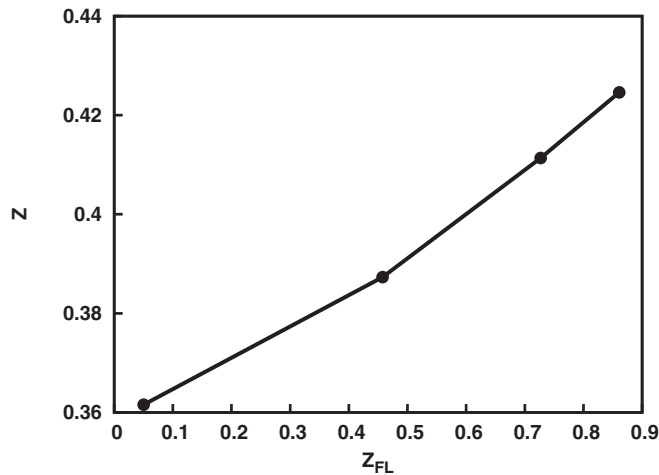
FIG. 13. Comparison of the screening charge Z with the Fermi-liquid renormalization factor Z_{FL} in two-dimensional systems with $V_0 = 8t$.

remains finite in the Mott insulator where FOs are absent (cf. the lower panel of Fig. 12) (see Appendix C). The reason is that at the impurity site $\vec{R}_{i_0}$ and in its vicinity the particle density is different from $\bar{n}_{\text{hom}}$ for any finite V_0 (see Fig. 9). Therefore, the screening charge Z, which counts the particle deviations for all lattice sites in Eq. (18), is finite even if FOs in the asymptotic regime (very far from the impurity site) are absent.

In Fig. 13 we compare the screening charge Z with the Fermi-liquid renormalization factor Z_{FL} for the same interaction U. In this case, Z is calculated for $V_0 = 8t$ for 2D systems. We approximately find a linear mutual dependence of these quantities in the two-dimensional lattice.

B. Three-dimensional cubic lattice

We present our preliminary studies of FO on a small cubic lattice with a system size of $11 \times 11 \times 11$ with an impurity $V_0 = 6t$ placed at the center $(6a, 6a, 6a)$ of the cube. Simulating a larger lattice system (e.g., $21 \times 21 \times 21$) demands more sophisticated computational methods. In the present case we have only five sites away from the impurity in each direction. In Fig. 14 we show the particle density along the diagonal (a, a, a) direction. We substitute the value of densities at the impurity site by the second smallest values as in the 2D case. We see that the amplitude decreases with the interactions and approaches zero at the Mott transition $U_c = 15t$, which is in good agreement with the predictions from linearized DMFT [78]. We thus show some initial signatures of the disappearance of the FOs also in the 3D system. However, we cannot perform a decay analysis with just five lattice sites in one direction. Also, the interferences from the system boundaries (under periodic boundary conditions) make the screening charge for such a small system to be difficult to interpret at all. We have seen a similar behavior of the density at the impurity site with U and V for the 2D and 3D systems. It is left as an open question if we would also see this similarity in 2D and 3D systems for the FO decay and the behavior of the screening charge.
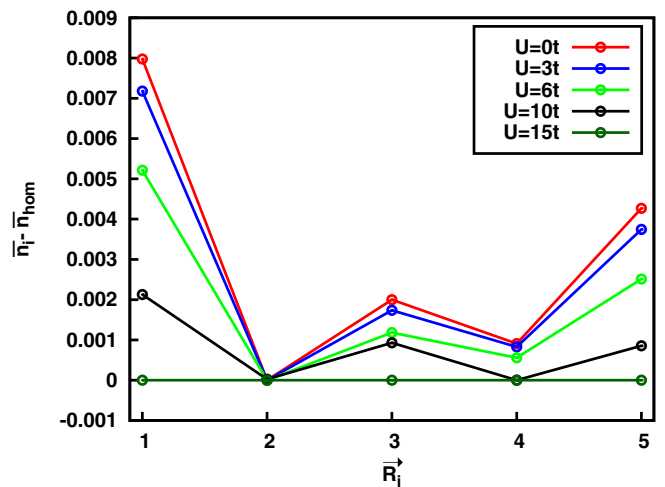

FIG. 14. The local occupations plotted along the diagonal (a, a, a) direction of the cubic lattice showing five sites: $\vec{R}_1 = (7a, 7a, 7a), \vec{R}_2 = (8a, 8a, 8a), \vec{R}_3 = (9a, 9a, 9a), \vec{R}_4 = (10a, 10a, 10a)$, and $\vec{R}_5 = (11a, 11a, 11a)$ for selected interactions. An impurity $V_0 = 6t$ is placed at the center of the cube, i.e., $(6a, 6a, 6a)$.

VI. CONCLUSIONS

We investigated the Friedel oscillations and screening effects around an impurity potential within the Hubbard model in finite lattices with a detailed study of 2D systems and a preliminary case study for 3D systems. The initial result of FO in 3D systems is a good starting point for understanding the FO in real materials with correlated electrons. We solved the Hubbard model within the real-space dynamical mean-field theory at finite and zero temperatures by using continuous-time quantum Monte Carlo simulations and homogeneous self-energy approximations with numerical renormalization group, respectively. In metallic, Fermi-liquid regime the Friedel oscillations are damped by increasing the interaction but their decaying pattern $1/r^d$ is the same as in the noninteracting ideal Fermi gas. We found that decaying of amplitude oscillations follows the behavior of the Fermi-liquid renormalization factor, which decreases with increasing the interaction. The same holds here for the screening charge. We also observed that the lifetime of the Fermi-liquid quasiparticles, which vanishes at the metal-insulator transition point, does not play an essential role in understanding the behavior of Friedel oscillations. In the Mott insulating phase the Friedel oscillations, very far from the impurity potential, are absent. Only very close to the impurity site there are deviations in the density with respect to homogeneous systems. The screening charge remains finite in the insulator. We found very good agreement on a qualitative and even quantitative level between the exact Monte Carlo simulations and the homogeneous self-energy approximations, as presented in Appendix C. We thus conclude that the homogeneous self-energy approximation, which is much cheaper in computational time and cost, is a reliable approximation for the present problems. We also obtained initial results for Friedel oscillations in cases of few impurities in the system where interesting interference effects are seen. These results deserve a separate publication.

VII. OUTLOOK AND PROPOSITION FOR FUTURE EXPERIMENTS

This study is planned to be extended into three-dimensional systems with larger number of lattice sites to confirm the asymptotic $1/r^3$ behavior in the amplitude decaying of Friedel oscillations. It is interesting to know if this decay is isotropic and how the screening behaves with changing the interaction. For this the real-space dynamical mean-field theory either within the Monte Carlo simulations or within the numerical renormalization group method should be parallelized and the computational task should be split on many computing nodes.

The Mott transition in two-dimensional Hubbard model cannot be completely described within the single-site DMFT approximation where the short-ranged spatial correlation is neglected [81]. As a future work it can be investigated how our results on the behavior of FO around the Mott transition for a 2D Hubbard model would change with the inclusion of spatial correlations beyond the single-site DMFT approximation. Our results can further motivate more involved studies like behavior of the FO in the pseudogap regime before the Mott transition in a 2D Hubbard model where the quasiparticles disappear in the so-called antinodal region of the momentum space, taking into account the effects of nonlocal correlations.

It is interesting to probe if FO can be observed in real Mott insulators (e.g., transition metal oxides like NiO, V_2O_3, $SrVO_3$, $LaTiO_3$, etc.) in the presence of dopants adsorbed at the surface and/or surface defects. A pressure-induced Mott transition has been observed in the transition metal oxide Fe_2O_3 combining methods of Mossbauer spectroscopy, x-ray diffraction, and electrical resistance [82]. The same has been recently theoretically modeled and seen by using the DMFT+DFT (density functional theory) [83]. A Mott-Hubbard transition in heterostructures of correlated oxides using DFT+DMFT has been presented in [84]. It is interesting to see if FOs due to the local defects affect the charge transport properties, e.g., transport current, resistance across the interface of such heterostructures. Studies of Mott localization in nanostructures with magnetic impurities with an extended nano-DMFT have been discussed in [85]. These studies can be extended including dopants/impurities in the system to investigate signature of FO in real Mott systems. Transition metal oxides are the prospective functional materials for the class of future electronic devices called Mott transistors or often referred to as Mottronics which would be based on the charge correlations between the electrons. Such devices would find their application as an on/off switch, mem-resistors, etc. Experimentally tailoring materials for such devices and measuring the transport properties like the temperature-dependent resistivity is an emerging field of research [86,87]. It is a relevant point to investigate if the FOs influence the electrical conductance, resistivity, transport current, and other transport properties of such Mottronic devices by producing local quantum ripples and noises due to the presence of local defects/impurities. Any signature of FOs in the output characteristics of these devices may be used as an indicator to spot local defects and their role in affecting the performance of the same. The FOs may be detected in probing the surfaces with scanning tunneling microscopy (STM) like in the case of [88]. Our model calculations should motivate new experiments and *ab initio* calculations on real materials along this direction.

APPENDIX A: ESTIMATION OF THE U_{c1} AND U_{c2} FOR THE "1D TOY MODEL" USING R-DMFT+ CT-QMC

We study the Mott transition for the 1D Hubbard model at finite temperature within R-DMFT + CT-QMC following the numerical scheme presented in [80]. According to our calculations, $\beta = 5/t$ is above the critical temperature while $\beta = 20/t$ is below the critical temperature where the coexistence region separates the metallic from the insulating phase (cf. Fig. 15). We estimate the two transition points $U_{c1} = 6.6t, U_{c2} = 7.2t$ by examining the behavior of the double occupancy ($\langle d_0 \rangle$) with the interactions as shown in Fig. 15 (lower panel). $\langle d_0 \rangle$ is directly obtained from the CT-QMC calculations. $\langle d_0 \rangle$ decreases as U increases showing a discontinuous jump to a lower value at a certain interaction strength U_{c2} when the system becomes insulating. Again, as the interaction is decreased from the insulating solution, another discontinuous jump is seen in d_0, at an interaction strength U_{c1} which is slightly lower than U_{c2}.

APPENDIX B: TECHNICAL DETAILS OF CT-QMC SOLVER

We present some technical details of the CT-QMC solver developed by us based on the approach of Haule [74]. For each physical set of parameters (U, β) we solve the R-DMFT equations iteratively. We assume that the solution is achieved, if a difference between the Green's functions $G(\tau)$ in the last four iterations is lower than our preassigned convergence (conv) parameter. In our calculations the Green's function $G(\tau)$ used in the above convergency condition is calculated by taking the Fourier transform from $G(i\omega_n)$. $G(i\omega_n)$ is determined by our quantum Monte Carlo hybridization expansion solver for the maximal number of Matsubara frequencies ω_n given by $N_{\max}$ [74], while its asymptotic form for large $|\omega_n|$ up to $|\omega_n|^3$ is determined analytically [89]. The solver detemines $G(i\omega_n)$ and their respective stochastic errors. Each time the solver is used we check whether the Green's function for the highest calculated Matsubara frequency agrees with its asymptotic form. If not, we increase $N_{\max}$ until this agreement is achieved.
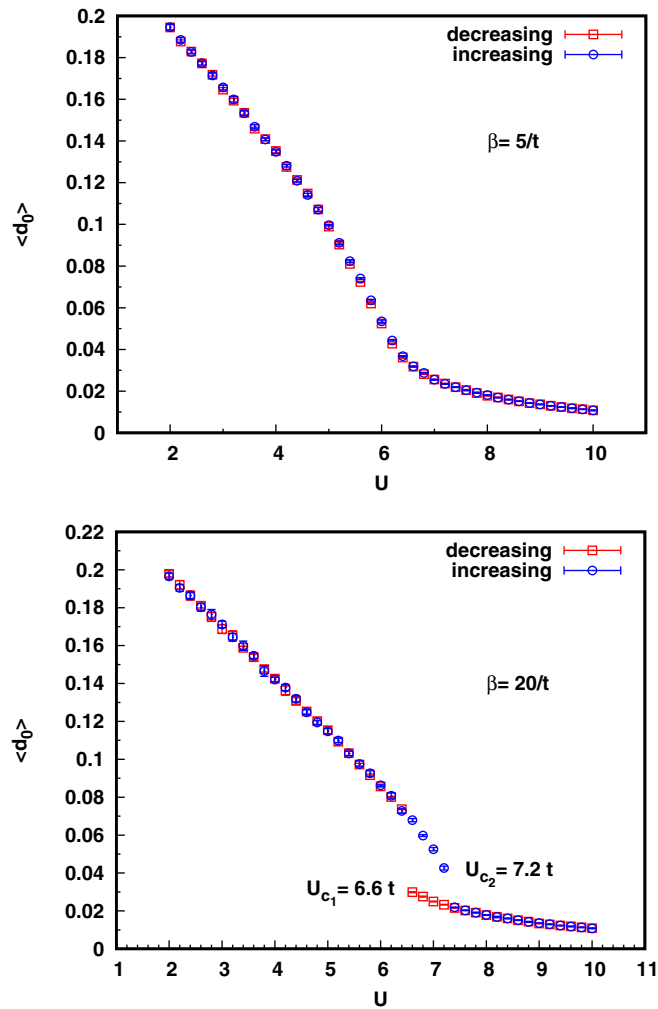
FIG. 15. Variation of the double occupancy (d_0) with the interaction (U) at the temperature $\beta = 5/t$ (upper panel), $\beta = 20/t$ (lower panel) for a homogeneous 1D lattice chain within the R-DMFT+CT-QMC method. The data from the DMFT solutions obtained by decreasing and increasing U are marked with the red and blue points, respectively.
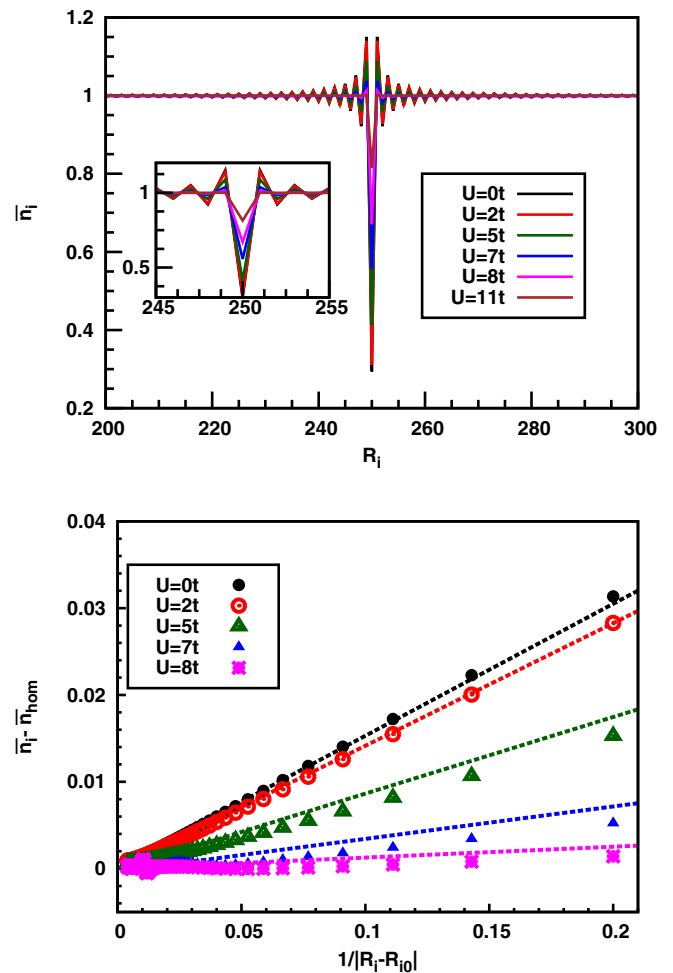

FIG. 16. (Upper panel) Friedel oscillations in particle densities at different lattice sites in presence of the single-impurity potential $V_0 = 2t$ placed at $R_i = 250a$ in a 1D chain with $N_L = 500$ sites. Different colors correspond to different interactions U which are accounted for by using R-DMFT within HSEA. The insets show FOs in the neighborhood of the impurity. (Lower panel) Variation of the local density deviations as a function of inverse of the relative distance from the impurity site for the same. (Compare with Figs. 3 and 5 for the equivalent CT-QMC results.)

After every subsequent iteration we also increase the number of Monte Carlo steps N_{MC} used in the CT-QMC solver. N_{max} and N_{MC} are monitored individually for each lattice site.

If N_{max} or N_{MC} increases, then the computational time also increases. As explained by Haule for lower temperatures higher and higher orders must be probed in the hybridization expansion [74]. We observe this behavior also in our calculations. In our case, one iteration lasts around 3 h for our 1D toy model with $N_L = 50$ ($\beta = 20/t$, $U = 6t$, conv = 0.005) and around 8 h for the 2D 31×31 lattice ($\beta = 15/t$, $U = 8t$, and conv = 0.01). These representative values substantiate the fact that achieving results for the 2D systems for low-temperature, high interactions with a greater accuracy is computationally nontrivial. In general it is difficult to reach a convergent solution for high interactions. Each time we restarted the calculations for high-U values from the already converged solution of the low-U values. Yet, achieving physically convergent solution for very high U (in the insulating regime) was nontrivial unlike in the case of HSEA.

APPENDIX C: COMPARISON BETWEEN R-DMFT+CT-QMC AND HSEA FOR THE 1D TOY MODEL

We present the analogy and the qualitative agreement between the exact Monte Carlo and the HSEA for the 1D toy model. Thereby, we claim that the HSEA is also a reliable approximation for studying FOs in higher-dimensional lattices.

In Fig. 16 (upper panel) we present the density $\bar{n}_i$ on different lattice sites where $N_L = 500$ sites and when the impurity potential $V_0 = 2t$ is set on the $R_i = 250a$ site. Within the HSEA we are able to work within much larger lattices as compared to the case of CT-QMC. Results are presented for different interactions U marked by lines in different colors. In the zoomed areas we show FO in the vicinity of the impurity site. Away form the impurity site the relative changes in the densities are very small, much lower than 1% even at $T = 0$. With increasing U the FOs are weaker and disappear
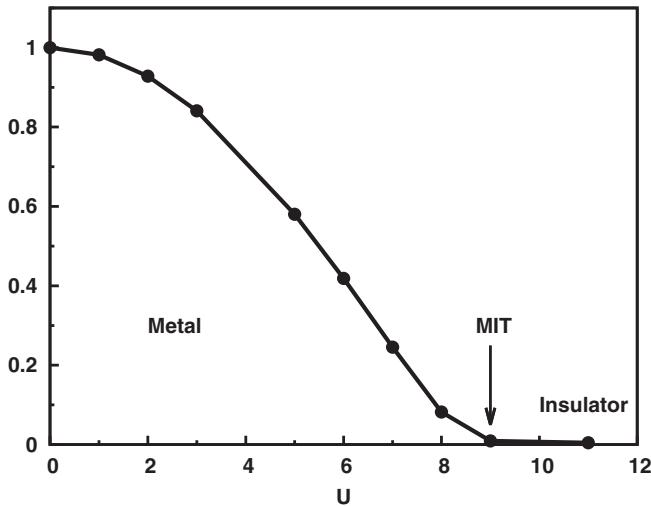
FIG. 17. Variation of the relative slope $A(U)/A(0)$ determined from Fig. 16 as a function of U and $A(0) = 0.154$. The other system parameters are the same as in Fig. 16. (Compare with Fig. 6 for the equivalent CT-QMC results.)
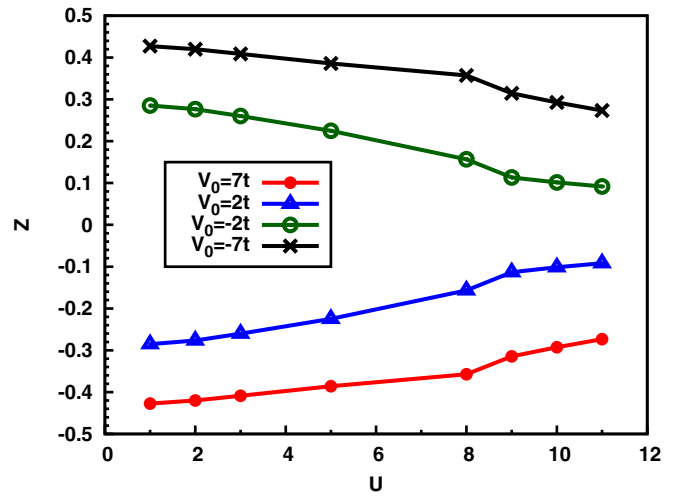

FIG. 18. Screening charge Z determined from Eq. (18) as a function of the interaction U for $V_0 = \pm 2t$ and $\pm 7t$ (lower panel). The other system parameters are the same as in Fig. 16. [Compare with Fig. 7 (upper panel) for the equivalent CT-QMC results.]

completely when $U > U_c$, where U_c is the critical interaction where the Mott-Hubbard MIT occurs. In Fig. 16 (lower panel) we plot the local density deviations $|\bar{n}_i - \bar{n}_{\mathrm{hom}}|$ as a function of the inverse of the relative distance from the impurity site, i.e., $1/|R_i - R_{i_0}|$, where $R_{i_0} = 250a$. The asymptotic linear decay is visible in agreement with Eq. (1) in the presence of interactions. The points shown in Fig. 16 (lower panel) follow the approximate linear rule $|\bar{n}_i - \bar{n}_{\mathrm{hom}}| = Ax + B$, where $x = 1/|R_i - R_{i_0}|$ and the parameters A and B are determined by fitting procedure. In particular, the slope parameter $A = A(U)$ describes changes in the FO amplitude with U. We see that the slope $A(U)$ decreases with increasing U and vanishes at the metal-insulator transition (cf. Fig. 17) at $U_c \approx 9t$. The critical value U_c determined from the $A(U)$ curve is in perfect agreement with the linearized DMFT [78]. We see all these behaviors qualitatively agree with the CT-QMC results (cf. Figs. 3, 5, and 6 for comparison). However, the value of U_c is larger than that obtained within CT-QMC ($U_{c1} = 6.6t$, $U_{c2} = 7.2t$), and the curve has a convex nature as compared to the concave behavior in CT-QMC, but again $A(0)$ is around 0.154 in both the cases. While the larger value of U_c can be

justified as an effect of zero temperature (strictly speaking, $\beta = 10\,000/t$) in this case, it is difficult to address the reason behind the convex/concave nature of the decay curves in the two cases. This could be an effect of either the finite temperature, or the homogeneous self-energy approximation, or the use of different solvers. A more specific comment on this point is beyond the scope of the current calculations.

The screening charge Z, defined in Eq. (18), is shown in Fig. 18. On comparing it with the equivalent CT-QMC case in Fig. 7 (upper panel) we see that in both the cases Z decreases with U and shows a change in the behavior at the Mott transition. In case of CT-QMC for a low temperature $\beta = 15/t$, Z actually becomes zero beyond the Mott transition while in case of the HSEA some small finite residual screening charge is seen which could be due to the HSEA wherein additional contribution from the inhomogeneous part of the self-energy is neglected. Nevertheless, HSEA reproduces the qualitative behavior of Z with U and arrives at the common conclusion that interaction weakens screening, confirming its reliability in also studying Z in distances close to the impurity.

[1] J. Friedel, Philos. Mag. **43**, 153 (1952).

[2] J. Friedel, Nuovo Cimento Suppl. **7**, 287 (1958).

[3] C. Kittel, *Quantum Theory of Solids* (Wiley, New York, 1963).

[4] F. García-Molinear, Quantum-mechanical techiniques, in *Theory of Imperfect Crystalline Solids: Trieste Lectures 1970* (International Atomic Energy Agency, Vienna, 1971), p. 1–100.

[5] J. Villain, M. Lavagna, and P. Bruno, C. R. Phys. **17**, 276 (2016).

[6] É. Daniel, C. R. Phys. **17**, 291 (2016).

[7] C. Benta, C. R. Phys. **17**, 302 (2016).

[8] A. Georges, C. R. Phys. **17**, 430 (2016).

[9] D. M. Eigler and E. K. Schweizer, Nature (London) **344**, 524 (1990).

[10] M. F. Crommie, C. P. Lutz, and D. M. Eigler, Science **262**, 218 (1993).

[11] E. J. Heller, M. F. Crommie, C. P. Lutz, and D. M. Eigler, Nature (London) **369**, 464 (1994).

[12] H. C. Manoharan, C. P. Lutz, and D. M. Eigler, Nature (London) **403**, 512 (2000).

[13] G. Binnig, H. Rohrer, Ch. Gerber, and E. Weibl, Appl. Phys. Lett. **40**, 178 (1982); Phys. Rev. Lett. **49**, 57 (1982); **50**, 120 (1983).

[14] K. Kanisawa, M. J. Butcher, H. Yamaguchi, and Y. Hirayama, Phys. Rev. Lett. **86**, 3384 (2001).

[15] Y. Hasegawa, M. Ono, Y. Nishigata, T. Nisho, and T. Eguchi, J. Phys.: Conf. Ser. **61**, 399 (2007).

[16] M. Bouhassoune, B. Zimmermann, P. Mavropoulos, D. Wortmann, P. H. Dederichs, S. Blugel, and S. Lounis, Nat. Commun. **5**, 5558 (2014).

[17] P. Sessi, V. M. Silkin, I. A. Nechaev, Th. Bathon, L. El-Kareh, E. V. Chulkov, P. M. Echenique, and M. Bode, Nat. Commun. **6**, 8691 (2015).

[18] K. W. Clark, X-G. Zhang, G. Gu, J. Park, G. He, R. M. Feenstra, and A.-P. Li., Phys. Rev. X **4**, 011021 (2014).

[19] A. M. Clogston, Phys. Rev. **125**, 439 (1962).

[20] J. Callaway, J. Math. Phys. **5**, 783 (1964).

[21] I. Adawi, Phys. Rev. **146**, 379 (1966).

[22] J. Rudnick and E. A. Stern, Phys. Rev. B **7**, 5062 (1973).

[23] A. M. Gabovich, L. G. II'chenko, E. A. Pashitskii, and Y. A. Romanov, Zh. Eksp. Teor. Fiz. **75**, 249 (1978) [Sov. Phys.– JETP **48**, 124 (1978)].

[24] F. Flores and A. M. Stoneham, J. Phys. Chem. Solids **40**, 531 (1979).

[25] G. D. Mahan, Int. J. Mod. Phys. **09**, 1313 (1995); **9**, 1327 (1995).

[26] S. Lounis, P. Zahn, A. Weismann, M. Wenderoth, R. G. Ulbrich, I. Mertig, P. H. Dederichs, and S. Blügel, Phys. Rev. B **83**, 035427 (2011).

[27] O. P. Sinha, Am. J. Phys. **38**, 996 (1970).

[28] I. Affleck, L. Borda, and H. Saleur, Phys. Rev. B **77**, 180404(R) (2008).

[29] Y. Tao and G. Bergmann, Eur. Phys. J. B **85**, 42 (2012).

[30] A. K. Mitchell, P. G. Derry, and D. E. Logan, Phys. Rev. B **91**, 235127 (2015).

[31] P. G. Derry, A. K. Mitchell, and D. E. Logan, Phys. Rev. B **92**, 035126 (2015).

[32] R. Egger and H. Grabert, Phys. Rev. Lett. **75**, 3505 (1995); in *Quantum Transport in Semiconductor Submicron Structures*, edited by B. Kramer NATO-ASI Series E (Kluwer, Dordrecht, 1996).

[33] A. Leclair, F. Lesage, and H. Saleur, Phys. Rev. B **54**, 13597 (1996).

[34] R. Egger and H. Grabert, Phys. Rev. Lett. **79**, 3463 (1997).

[35] G. Bedürftig, B. Brendel, H. Frahm, and R. M. Noack, Phys. Rev. B **58**, 10225 (1998).

[36] V. I. Fernández and C. M. Naón, Phys. Rev. B **64**, 033402 (2001).

[37] G. F. Giuliani, G. Vignale, and T. Datta, Phys. Rev. B **72**, 033411 (2005).

[38] D. F. Urban and A. Komnik, Phys. Rev. Lett. **100**, 146602 (2008).

[39] W. Ziegler, H. Endres, and W. Hanke, Phys. Rev. B **58**, 4362 (1998).

[40] J. K. Freericks, Phys. Rev. B **70**, 195342 (2004).

[41] P. Lederer and M. Rozenberg, Europhys. Lett. **81**, 67002 (2008).

[42] E. C. Andrade, E. Miranda, and V. Dobrosavljević, Phys. Rev. Lett. **104**, 236401 (2010).

[43] D. F. Mross and T. Senthil, Phys. Rev. B **84**, 041102(R) (2011).

[44] B. Chatterjee and K. Byczuk, J. Phys.: Conf. Ser. **592**, 012059 (2015).

[45] J. Kroha, A. Huck, and T. Kopp, Phys. Rev. Lett. **75**, 4278 (1995)

[46] T. D. Stanescu and V. Galitski, Phys. Rev. B **74**, 205331 (2006).

[47] M.-T. Tran and K.-S. Kim, Phys. Rev. B **82**, 155142 (2010).

[48] W. E. Liu, H. Liu, and D. Culcer, Phys. Rev. B **89**, 195417 (2014).

[49] V. V. Cheianov and V. I. Falko, Phys. Rev. Lett. **97**, 226801 (2006).

[50] E. H. Hwang and S. Das Sarma, Phys. Rev. Lett. **101**, 156802 (2008).

[51] A. Bácsi and A. Virosztek, Phys. Rev. B **82**, 193405 (2010).

[52] K. Riechers, K. Hueck, N. Luick, T. Lompe, and H. Moritz, Eur. Phys. J. D **71**, 232 (2017).

[53] A. Vanyolos, B. Dora, and A. Virosztek, Phys. Rev. B **75**, 193101 (2007).

[54] A. Gorczyca, M. M. Maśka, and M. Mierzejewski, Rev. B **76**, 165419 (2007).

[55] E. G. Dalla Torre, D. Benjamin, David, Y. He, D. Dentelski, and E. Demler, Phys. Rev. B **93**, 205117 (2016).

[56] M. A. Ruderman and C. Kittel, Phys. Rev. **96**, 99 (1954).

[57] T. Kasuya, Prog. Theor. Phys. **16**, 45 (1956).

[58] K. Yosida, Phys. Rev. **106**, 893 (1957).

[59] I. Titvinidze, A. Schwabe, N. Rother, and M. Potthoff, Phys. Rev. B **86**, 075141 (2012).

[60] J. S. Langer and V. Ambegaokar, Phys. Rev. **121**, 1090 (1961).

[61] D. C. Langreth, Phys. Rev. **150**, 516 (1966).

[62] R. M. Martin, Phys. Rev. Lett. **48**, 362 (1982).

[63] K. Byczuk, B. Chatterjee, and D. Vollhardt, Eur. Phys. J. B **92**, 23 (2019).

[64] V. Dobrosavljević and G. Kotliar, Phys. Rev. Lett. **78**, 3943 (1997).

[65] M. Potthoff and W. Nolting, Phys. Rev. B **59**, 2549 (1999); **60**, 7834 (1999).

[66] S. Okamoto and A. J. Millis, Phys. Rev. B **70**, 241104(R) (2004).

[67] R. W. Helmes, T. A. Costi, and A. Rosch, Phys. Rev. Lett. **100**, 056403 (2008); **101**, 066802 (2008).

[68] M. Snoek, I. Titvinidze, C. Toke, K. Byczuk, and W. Hofstetter, New J. Phys. **10**, 093008 (2008).

[69] K. Byczuk, in *Condensed Matter Physics In The Prime Of The 21st Century: Phenomena, Materials, Ideas, Methods*, edited by J. Jedrzejewskii (World Scientific, Singapore, 2008), pp. 1.

[70] W. Metzner and D. Vollhardt, Phys. Rev. Lett. **62**, 324 (1989).

[71] A. Georges, G. Kotliar, W. Krauth, and M. J. Rozenberg, Rev. Mod. Phys. **68**, 13 (1996).

[72] J. W. Negele and H. Orland, *Quantum Many-particle Systems* (Westview, Boulder, CO, 1988).

[73] E.l Gull, A. J. Millis, A. I. Lichtenstein, A. N. Rubtsov, M. Troyer, and P. Werner, Mod. Phys. **83**, 349 (2011).

[74] K. Haule, Phys. Rev. B **75**, 155113 (2007).

[75] R. Bulla, T. A. Costi, and T. Pruschke, Rev. Mod. Phys. **80**, 395 (2008).

[76] For more information on the code consult the software web page http://nrgljubljana.ijs.si

[77] T. Schäfer, F. Geles, D. Rost, G. Rohringer, E. Arrigoni, K. Held, N. Blümer, M. Aichhorn, and A. Toschi, Phys. Rev. B **91**, 125109 (2015).

[78] R. Bulla and M. Potthoff, Eur. Phys. J. B **13**, 257 (2000).

[79] E. H. Lieb and F. Y. Wu, Phys. Rev. Lett. **20**, 1445 (1968).

[80] A. J. Kim, M. Y. Choi, and G. S. Jeon, J. Korean Phys. Soc. **64**, 268 (2014).

[81] G. Kotliar, S. Y. Savrasov, K. Haule, V. S. Oudovenko, O. Parcollet, and C. A. Marianetti, Rev. Mod. Phys. **78**, 865 (2006).

[82] M. P. Pasternak, G. K. Rozenberg, G. Y. Machavariani, O. Naaman, R. D. Taylor, and R. Jeanloz, Phys. Rev. Lett. **82**, 4663 (1999).

[83] E. Greenberg, I. Leonov, S. Layek, Z. Konopkova, M. P. Pasternak, L. Dubrovinsky, R. Jeanloz, I. A. Abrikosov, and G. K. Rozenberg, Phys. Rev. X **8**, 031059 (2018).

[84] Z. Zhong, M. Wallerberger, J. M. Tomczak, C. Taranto, N. Parragh, A. Toschi, G. Sangiovanni, and K. Held, Phys. Rev. Lett. **114**, 246401 (2015).

[85] S. Florens, Phys. Rev. Lett. **99**, 046402 (2007).

[86] P. Maier, F. Hartmann, J. Gabel, M. Frank, S. Kuhn, P. Scheiderer, B. Leikert, M. Sing, L. Worschech, R. Claessen, and S. Höfling, Appl. Phys. Lett. **110**, 093506 (2017).

[87] P. Scheiderer, M. Schmitt, J. Gabel, M. Zapf, M. Stübinger, P. Schütz, L. Dudy, C. Schlueter, T.-L. Lee, M. Sing, and R. Claessen, Adv. Mater. **30**, 1706708 (2018).

[88] Y. Okada, S.-Y. Shiau, T.-R. Chang, G. Chang, M. Kobayashi, R. Shimizu, H.-T. Jeng, S. Shiraki, H. Kumigashira, A. Bansil, H. Lin, and T. Hitosugi, Phys. Rev. Lett. **119**, 086801 (2017).

[89] W. Nolting, *Fundamentals of Many-body Physics* (Springer, Berlin, 2008).